Scientific Reports

https://doi.org/10.1038/s41598-026-46548-0

Article in Press

Developing antibacterial Zn-Cu-Mg alloys with high strength and osteogenic stimulation for osteomyelitis

Received: 22 December 2025

Accepted: 26 March 2026

Published online: 02 April 2026

Cite this article as: He J., Song Y., Xiao Y. *et al.* Developing antibacterial Zn-Cu-Mg alloys with high strength and osteogenic stimulation for osteomyelitis. *Sci Rep* (2026). https://doi.org/10.1038/s41598-026-46548-0

Jingzhe He, Yindong Song, Yi Xiao, Yifan Wang, Yuan Yan, Hui Yu, Yu Zhang, Guiying Liu & Jin Xiao

Developing Antibacterial Zn-Cu-Mg Alloys with High Strength and Osteogenic Stimulation for Osteomyelitis

Jingzhe He [a, #], *Yindong Song* [b, #], *Yi Xiao* [c], *Yifan Wang* [d], *Yuan Yan* [a], *Hui Yu* [a], *Yu Zhang* [a, *], *Guiying Liu* [e, *], *Jin Xiao* [f, *]

Author affiliations:

[a] Department of Orthopaedics Oncology, Guangdong Provincial People's Hospital (Guangdong Academy of Medical Sciences), Southern Medical University, Guangzhou, Guangdong 519041, P.R. China.

[b] Department of Orthopedics, Liwan Central Hospital of Guangzhou, Guangzhou, Guangdong 510170, P.R. China.

[c] Division of Orthopaedic Surgery, Department of Orthopaedics, Nanfang Hospital, Southern Medical University, Baiyun Distrcit, Guangzhou, Guangdong 510515, China

[d] Department of Orthopaedic Surgery, The Third People's Hospital of Chengdu, Chengdu, Sichuan 610031, P.R. China.

[e] Department of Cardiovasology, The Fifth Affiliated Hospital of Southern Medical University, No. 566 Congcheng Avenue, Conghua District, Guangzhou, Guangdong 510900, P. R. China.

[f] Department of Orthopedics, Guangdong Provincial People's Hospital (Guangdong Academy of Medical Sciences), Maoming People's Hospital, Southern Medical University, Guangzhou, Guangdong 510080, P. R. China.

[#] These authors contributed equally: Jingzhe He, Yindong Song.

* Corresponding author: Jin Xiao: xiaojinhn@163.com, Guiying Liu: Liugy1987@163.com, Yu Zhang, luck_2001@126.com.

Abstract

Biodegradable metals are promising candidates for osteomyelitis management because they can provide mechanical support, enable tunable degradation, display inherent antibacterial effects, and stimulate osteogenesis. Here, Zn alloys incorporating Cu and Mg were designed as multifunctional implant materials to concurrently suppress infection and promote bone regeneration. Equal channel angular pressing (ECAP) was used to refine grains to the submicron scale and substantially fragment secondary phases. Mechanical testing showed that Zn-1Cu-1Mg alloy achieved the highest hardness and tensile strength among the investigated alloys, which is attributed to the combined contributions of grain refinement and second-phase strengthening. Electrochemical and immersion evaluations further indicated that the addition of Cu improved corrosion resistance of Zn-1Mg alloy. The reduced corrosion rate is associated with the formation of compact corrosion layers enriched in Zn, O, C, Ca, P, and Cl. In vitro assays using BMSCs demonstrated high cell viability, meanwhile, osteogenic assessments revealed enhanced ALP activity, increased mineralized nodule formation, and upregulated osteogenic gene expression. All Zn alloys also showed pronounced antibacterial activity against *S. aureus* and *E. coli*. Collectively, these results suggest that Zn-1Cu-1Mg alloys offer a multifunctional biodegradable option for osteomyelitis through the integration of infection control and bone regeneration.

Keywords: Zinc alloy; Mechanical properties; Corrosion; Osteogenesis; Antibacterial activity

1. Introduction

Osteomyelitis is a severe, persistent inflammatory disorder of bone tissue that is most commonly caused by bacterial infection, with *Staphylococcus aureus* as the predominant pathogen [1,2]. Despite advances in surgical techniques and antimicrobial therapy, clinical management remains difficult because of intrinsic disease features, including bacterial colonization of bone and implants, biofilm formation, extensive bone destruction, chronic inflammation, and impaired bone regeneration [3]. The rising prevalence of antibiotic-resistant strains further limits treatment efficacy, underscoring the need for alternative strategies. Conventional care, typically combining systemic antibiotics with surgical debridement, often fails to fully eradicate infection and restore functional bone integrity. Therefore, implant materials are needed that can provide mechanical stability while inhibiting bacterial growth, modulating the local microenvironment, and promoting new bone formation.

Biodegradable metals have attracted increasing interest as next-generation biomaterials because they gradually degrade and can be replaced by regenerated tissue, potentially eliminating the need for secondary removal surgery [4-6]. Magnesium (Mg) and iron base systems have been widely investigated, but both have inherent drawbacks. Magnesium degrades rapidly and produces hydrogen gas, which can compromise mechanical stability and tissue integration [7,8]. In contrast, iron corrodes too slowly for many clinical applications [9,10]. Zinc (Zn) and its alloys have recently emerged as a promising third class of biodegradable metals, offering moderate corrosion rates, release of essential trace ions, favorable biocompatibility, and substantial room for alloy design [11-13]. Notably,

zinc contributes to bone metabolism, immune regulation, and antibacterial defense, making Zn-based alloys particularly appealing for orthopedic use [14-16].

However, pure Zn has limited mechanical strength and inadequate antibacterial activity, restricting its use in load-bearing settings and infection-related bone diseases [17]. Alloying Zn with biologically relevant elements such as copper (Cu) and Mg is an effective approach to address these limitations [18,19]. Cu provides broad-spectrum antibacterial activity by disrupting bacterial membranes, inhibiting key respiratory enzymes, and suppressing biofilm formation [20,21]. Mg enhances strength through solid-solution and precipitation strengthening, and its degradation releases Mg^{2+} ions that support osteogenic differentiation and extracellular matrix mineralization [22]. Despite the promising antibacterial and strengthening effects of Cu addition in Zn-based alloys, potential risks should also be considered [23,24]. Although Cu^{2+} ions exhibit antibacterial properties, elevated Cu ion concentrations may induce cytotoxic effects in mammalian cells. Therefore, precise control of Cu content and microstructural distribution is critical to avoid excessive ion release and to maintain biocompatibility. Co-alloying Zn with Cu and Mg offers a rational route to engineer multifunctional biomaterials that jointly meet the demands of infection control and bone regeneration for osteomyelitis treatment.

In addition to compositional engineering, microstructural refinement is critical for improving the performance of biodegradable metals. Equal-channel angular pressing (ECAP), a severe plastic deformation technique, enables the formation of ultrafine- or submicron-grained microstructures [25]. Such refinement typically increases strength, modifies corrosion behavior through a

higher grain-boundary density, and may influence cell–material interactions. Notably, copper's inclusion in Zn alloys not only enhances the antibacterial properties but also has a specific ability to penetrate and disrupt biofilms, a key challenge in osteomyelitis treatment [20]. Liu et al. investigated the evolution of Mg-containing phases in Zn–Mg alloys by varying ECAP passes and processing temperature [26]. When the grain size of Zn–0.033Mg was reduced to the submicron scale by ECAP, elongation exceeded 30% [27]. ECAP-processed Zn–Cu alloys have also been studied extensively. For example, Bednarczyk et al. refined Zn–0.5Cu to an average grain size of ~1 μm, enabling room-temperature superplasticity. High-Cu Zn–Cu alloys have likewise been reported to develop ultrafine-grained microstructures and achieve high elongation [28,29]. In addition, Yang *et al.* fabricated Zn–3Cu–1Mg alloys and examined the evolution of $CuZn_5$ and Mg_2Zn_{11} particles during ECAP, demonstrating simultaneous improvements in strength and ductility [30]. However, the recommended daily intake of Cu is only 0.9 mg/day for adults, indicating the necessity to decrease Cu content in Zn alloys to avoid the excess release of Cu ions [31]. In addition, despite the well-established benefits of ECAP for grain refinement and mechanical enhancement in Zn–Cu–Mg alloys, their corrosion behavior and biological performance—including cytocompatibility, osteogenic activity, and antibacterial efficacy—remain insufficiently explored.

Accordingly, this study systematically evaluates the microstructure, mechanical properties, corrosion behavior, cytocompatibility, osteogenic potential, and antibacterial performance of ECAP-processed Zn–Cu, Zn–Mg, and Zn–Cu–Mg alloys. By integrating these results, we identify Zn–1Cu–1Mg as a promising multifunctional biodegradable metal platform for osteomyelitis-

related applications. The in vitro evidence presented here supports the potential of Zn–Cu–Mg alloys to address key limitations of current biomaterials for treating infected bone defects.

2. Materials and Methods

2.1. Alloy preparation

High-purity Zn (99.99 wt.%), Cu (99.99 wt.%), and Mg (99.99 wt.%) were melted in a high-purity graphite crucible under a protective argon atmosphere to minimize oxidation. Four target compositions, Zn–1Cu, Zn–2Cu, Zn–1Mg, and Zn–1Cu–1Mg, were designed to impart antibacterial (Cu) and osteogenic (Mg) functionalities to the Zn matrix. The melts were cast into carbon crucibles to produce cylindrical ingots. The chemical compositions of the as-cast alloys were quantified by inductively coupled plasma–atomic emission spectroscopy (ICP-AES; iCAP6300, USA). As summarized in **Table. 1**, the measured compositions were close to the nominal values. After solidification, the ingots were cut into cubic shape with sizes of 20 mm × 20 mm× 45 mm by electrical discharge wire cutting machine. The cubic samples were homogenized at 330℃ for 24h to reduce solute segregation and improve microstructural uniformity. Subsequently, the homogenized Zn alloys were cooled to room temperature in the air.

Table. 1: Chemical compositions of the designed Zn alloys.

Samples	Elemental compositions (wt.%)		
	Mg	Cu	Zn
Zn-1Cu	/	0.991	Basal
Zn-2Cu	/	2.039	Basal
Zn-1Mg	0.986	/	Basal

Zn-1Cu-1Mg	1.025	0.994	Basal

The homogenized alloys were processed by equal-channel angular pressing (ECAP) using route Bc to refine the grain structure and enhance mechanical and corrosion performance [25]. The square cross section dies with 90° angle between channels and outer curvature with 0° angle are in ECAP molds. ECAP was conducted at different processing temperatures and numbers of passes, producing bulk specimens. The final deformation parameters were set as 12 passes and 100℃ to promote microstructural stability and ensure reproducible mechanical properties.

2.2 Microstructural characterization

Scanning electron microscopy (SEM; Thermo Fisher Scientific, USA) was employed to examine surface morphology and the distribution of alloyed phases in both as-cast and ECAP-processed samples. Specimens were mechanically ground using sequential SiC papers, polished, and then etched in a 4 vol.% nitric acid ethanol solution. SEM was also used to evaluate corrosion morphologies after immersion tests, both before and after removal of corrosion products. Elemental distributions and secondary phases were assessed by energy-dispersive X-ray spectroscopy (EDS) using point analyses and area mapping on selected regions. Electron backscatter diffraction (EBSD; Oxford Instruments, UK) was performed to quantify crystallographic orientation, grain-size distribution, dynamic recrystallization (DRX), and geometrically necessary dislocation (GND) density in ECAP-processed alloys. Prior to EBSD, specimens were ion-polished to obtain a high-quality surface. Transmission electron microscopy (TEM; JEOL, Japan) was used to resolve submicron features in ECAP-processed Zn–1Cu–1Mg. Thin

foils were prepared by mechanical thinning followed by ion milling, and selected-area electron diffraction (SAED) was collected to confirm the crystal structures of secondary phases.

2.3. Mechanical characterization

Vickers microhardness was measured using Micro Hardness Tester, performing at a 100 g load and a 15 s dwell time. Nine indentations were performed per specimen, and the average value was reported. Dog-bone tensile specimens were machined from the cubic samples according to ASTM E8. Tensile tests were conducted at room temperature using a universal testing machine at a strain rate of 1×10^{-3} s^{-1}. Engineering stress–strain curves were used to determine yield strength, ultimate tensile strength, and elongation to failure. Fracture surfaces were examined by SEM to identify dominant failure modes (e.g., ductile dimples) and to relate fracture morphology to microstructure and mechanical performance.

2.4. Corrosion behavior

Electrochemical and immersion tests of Zn alloys were conducted in the Hank's solution with pH of 7.4 ± 0.1 at 37 ± 0.5 ℃. Electrochemical measurements were carried out using an electrochemical workstation (CS350M; CorrTest, China) in a three-electrode configuration, with a platinum counter electrode, a saturated calomel reference electrode, and the specimen as the working electrode. The exposed surface area of Zn alloys was fixed at 1 cm^2. Open-circuit potential was recorded for 3600 s, followed by potentiodynamic polarization from −1.8 to −0.6 V at a scan rate of 0.1 $mV \cdot s^{-1}$. For immersion testing, specimens were immersed in Hank's solution for 30 days and the solution was refreshed every two days. The solution volume-to-exposed area ratio was maintained at 20 $mL \cdot cm^{-2}$ in accordance with ASTM G31. Corrosion product

morphologies were examined by SEM. After immersion, specimens were rinsed with distilled water and dried, then chemically cleaned in 200 g·L^{-1} chromium trioxide (CrO_3) solution to remove corrosion products. Weight loss was measured (n = 3) and corrosion rates were calculated using:

$$V_{corr} = \frac{\Delta m}{\rho A t}$$

Where Δm is mass loss, ρ is density, A is the exposed area, and t is the immersion time. The cleaned surfaces were subsequently re-examined by SEM to reveal the underlying corrosion patterns. For each type of Zn alloy, at least four samples were used for electrochemical and immersion tests.

2.5. Cell viability tests

Bone mesenchymal stem cells (BMSCs; Cell Bank, Chinese Academy of Sciences) were cultured in Dulbecco's Modified Eagle Medium (DMEM; Gibco) supplemented with 10% fetal bovine serum (FBS) at 37°C in a humidified atmosphere containing 5% CO_2. Cell viability was evaluated using the Cell Counting Kit-8 (CCK-8) in an indirect contact (extract) assay. Disc specimens were prepared using the same procedure as those used for immersion tests and exposed to ultraviolet light on a clean workbench for 24 hours for sterilization. In accordance with ISO 10993-12:2012, extracts were prepared by immersing discs (exposed area: 2.2 cm^2) in DMEM for 24 h at a surface area-to-medium volume ratio of 1.25 cm^2·mL^{-1}. The undiluted extracts (100%) and extracts diluted to 50% and 25% were prepared for subsequent testing. Ion concentrations in the extracts were quantified by inductively coupled plasma mass spectrometry (ICP-MS; Thermo Fisher Scientific, USA). BMSCs were seeded in 96-well plates at 2,000 cells per well and allowed to attach for 24 h. The

culture medium was then replaced with the diluted extracts, and cells were cultured for 3 days. Thereafter, 10 μL of CCK-8 reagent was added to each well, and absorbance at 450 nm was recorded after 2 h using a microplate reader (iMARK; Bio-Rad, USA).

Cytotoxicity was further assessed by live/dead staining. BMSCs were seeded in 96-well plates and cultured with Zn-alloy extracts for 24 h, with pure Ti as a negative control. After incubation, cells were washed with phosphate-buffered saline (PBS) and stained with Calcein AM (1 μM; Thermo Fisher Scientific, USA) and propidium iodide (PI; 2 μg·mL^{-1}; Thermo Fisher Scientific, USA) for 15 min at room temperature. Fluorescence images were acquired using an inverted fluorescence microscope (Olympus, Tokyo, Japan).

2.6. Osteogenesis-induction tests

BMSCs were seeded in 6-well plates at 6 × 10^4 cells per well. Upon reaching ~80% confluence, the medium was replaced with osteogenic induction medium containing 50% extract and refreshed every 48 h. Alkaline phosphatase (ALP) staining (day 7) and alizarin red S (ARS) staining (day 14) were performed to evaluate early osteogenic differentiation and matrix mineralization, respectively. Staining outcomes were documented using an optical microscope (Olympus, Tokyo, Japan).

Gene expression was analyzed by quantitative real-time PCR (qPCR). BMSCs were seeded in 6-well plates at 6 × 10^4 cells per well and, at ~80% confluence, cultured in osteogenic induction medium containing 50% extract for 10 days. Total RNA was isolated using the RNeasy Mini Kit (Qiagen), and RNA concentration and purity were determined. For each sample, 1 μg of RNA was reverse-transcribed to cDNA using SuperScript™ III Reverse Transcriptase (Thermo Fisher Scientific, USA). Reverse transcription was

performed at 65°C for 5 min, 4°C for 1 min, 50°C for 60 min, and 70°C for 15 min. qPCR was conducted using SYBR Premix Ex Taq II (Takara, Japan) with the following cycling conditions: 95°C for 30 s, followed by 40 cycles of 95°C for 5 s and 60°C for 30 s. The expression of osteogenesis-related genes (Runx2, OPN, and COL1) was normalized to GAPDH, and relative expression levels were calculated using the $^{2-\Delta\Delta}$Ct method. qPCR was performed using a real-time PCR system (model/manufacturer).

2.7. Antibacterial tests

Antibacterial activity against *Staphylococcus aureus* (*S. aureus*) and *Escherichia coli* (*E. coli*) was evaluated using a spread-plate assay. Pure Ti served as the control. *S. aureus* and *E. coli* were cultured at 37°C for 24 h with shaking (150 rpm) in tryptic soy broth (TSB) and Luria–Bertani (LB) broth, respectively. The bacteria were then subcultured on LB agar plates for 3–5 passages to ensure stable growth. Bacterial suspensions were adjusted to 5×10^7 CFU·mL^{-1}, and 1 mL was added to each well containing the specimens. After incubation, aliquots were serially diluted in PBS (100×), spread on LB agar plates, and incubated at 37°C for 24 h. Antibacterial rate (AR) was calculated as: AR = [(Nc - Ns) / Nc] × 100%, where Nc is the average colony count on pure Ti and Ns is the average colony count on the tested specimens.

2.8. Statistical analysis

Statistical analyses were performed using one-way analysis of variance (ANOVA) followed by Tukey's post hoc test. Data are presented as mean ± standard deviation (SD). Differences of $*p < 0.05$, $**p < 0.01$, $***p < 0.001$, and $****p < 0.0001$ were considered statistically significant and statistically highly significant, respectively.

3. Results

3.1. Microstructural evolutions

As shown in **Figure 1a**, the as-cast Zn alloys exhibited heterogeneous microstructures composed of a primary α-Zn matrix and dispersed secondary phases. The Zn–1Cu and Zn–2Cu alloys contained dendritic Cu-rich phases, which were identified as $CuZn_4$ based on the Zn–Cu phase diagram [32]. The Zn–1Mg alloy showed a continuous, network-like secondary phase surrounding Zn grains, whereas Zn–1Cu–1Mg additionally contained $CuZn_4$ phases. Consistent with prior reports, Zn–Mg alloys typically exhibit a lamellar eutectic structure comprising Mg_2Zn_{11} and Zn [26,30]. The EDS results (**Figure 1b** and **c**) confirmed that Cu and Mg were enriched in the dendritic phases of Zn–2Cu and the network-like phases of Zn–1Mg, respectively. In Zn–1Cu–1Mg, trace Cu was also detected within the eutectic regions (**Figure 1d**). After ECAP, all alloys displayed characteristic deformation bands aligned with the extrusion direction (**Figure 1e**), indicating substantial plastic deformation, grain refinement, and disruption of coarse intermetallic phases. Higher-magnification SEM images further verified grain refinement to the submicron scale. Overall, ECAP-induced microstructural refinement involved both grain subdivision and fragmentation/redistribution of secondary phases.

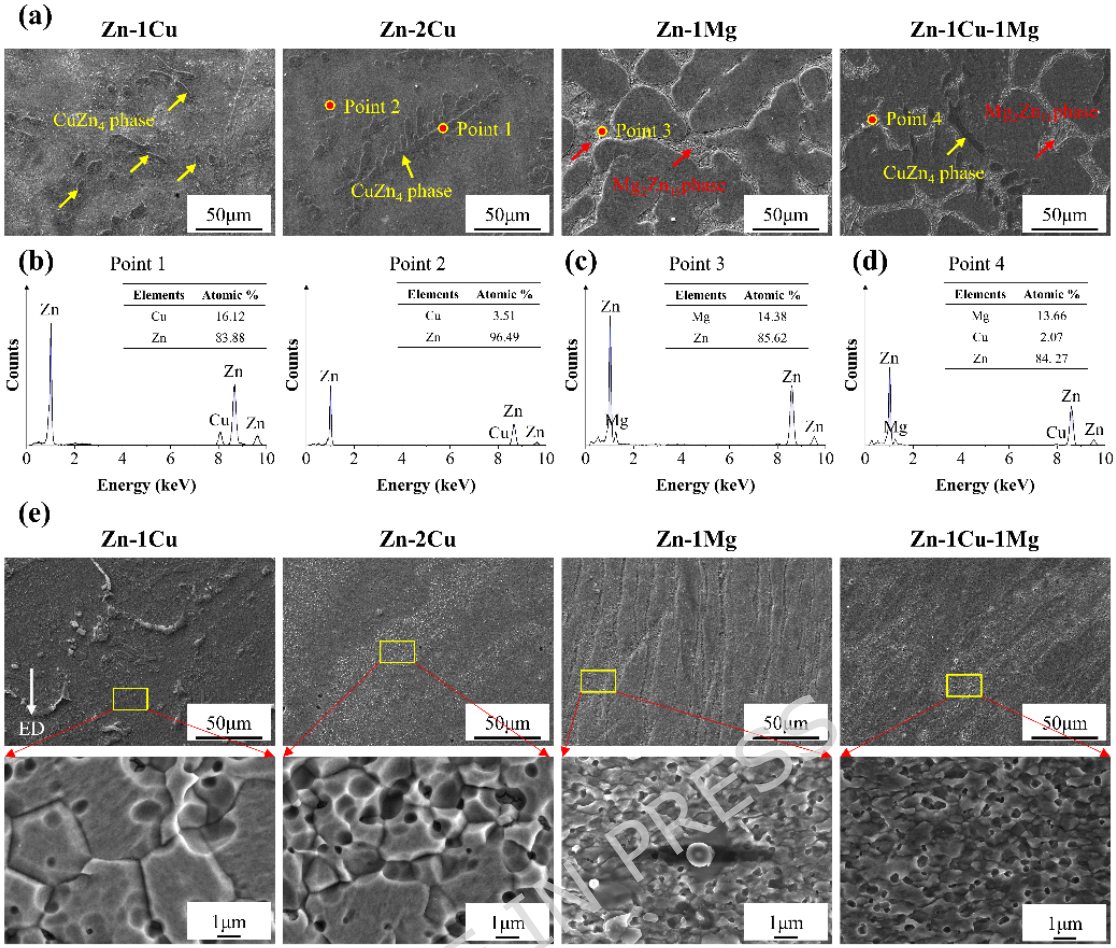

Figure 1: Microstructures of Zn alloys. (a) SEM images of as-cast Zn alloys. (b) EDS results of different regions in Zn-2Cu alloy. (c) EDS results of different regions in Zn-1Mg alloy. (d) EDS results of different regions in Zn-1Cu-1Mg alloy. (e) SEM images of as-deformed Zn alloys.

EBSD was employed to quantify grain orientation and size in the ECAP-processed alloys. The inverse pole figure (IPF) maps (**Figure 2a**) showed that the microstructures were dominated by dynamically recrystallized (DRX) grains with diverse orientations. As summarized in **Figure 2b**, the average grain size decreased from 1.06 μm in Zn–1Cu to 0.92 μm in Zn–2Cu, indicating enhanced refinement with increasing Cu content. Zn–1Mg exhibited an average grain size of 0.92 μm, which was further reduced to 0.58 μm after adding 1 wt.%

Cu (Zn–1Cu–1Mg). The fraction of submicron grains increased markedly, reaching 87% in Zn–1Cu–1Mg, suggesting that secondary phases effectively restricted DRX grain growth. The (0001) pole figures (**Figure 2c**) revealed pronounced textures; notably, Zn–1Cu exhibited the strongest basal texture, which is known to affect deformation mechanisms and anisotropy in HCP metals. The geometrically necessary dislocation (GND) maps (**Figure 2d**) indicated a lower GND density in Zn–1Cu–1Mg, consistent with its finer grain structure.

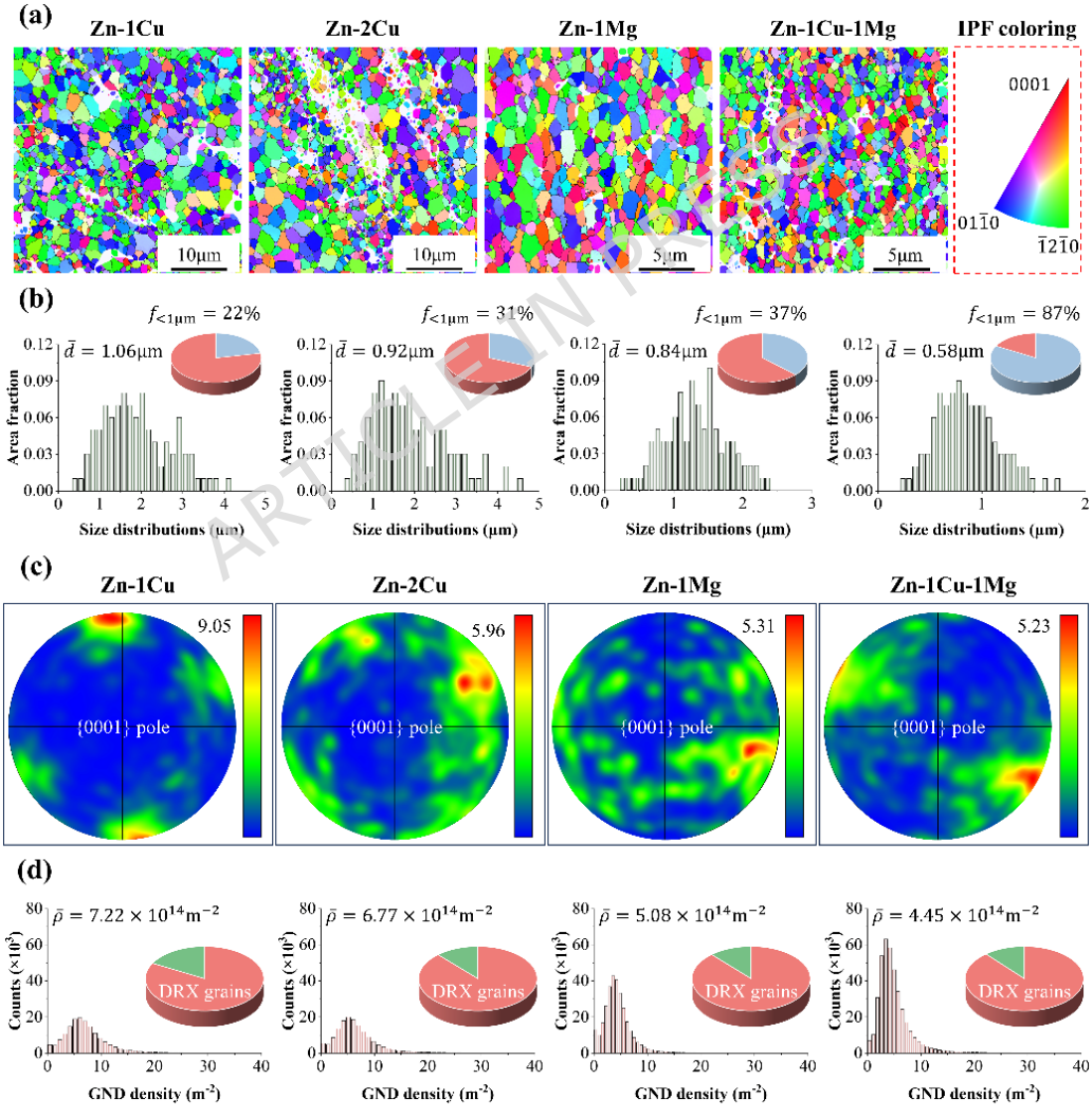

Figure 2: EBSD analysis of as-deformed Zn alloys. (a) IPF

images. (b) Grain size distributions and the fraction of small grains with sizes smaller than 1 μm. (c) 0001 PF images. (d) GND densities and the fractions of DRXed grains.

Texture variations directly influence the Schmid factor (SF) and, consequently, the activation of different slip systems. **Figure 3** summarizes SF distributions for the major slip systems in the ECAP-processed alloys. The average SF for basal ⟨a⟩ slip increased from 0.31 in Zn–1Cu to 0.34 in Zn–1Cu–1Mg. In contrast, prismatic ⟨a⟩ slip exhibited average SF values below 0.30 for all compositions, suggesting limited activation under the present loading orientation. The SF trends for pyramidal ⟨a⟩ slip were similar to those for basal ⟨a⟩ slip, with the lowest average value (~0.30) observed in Zn–1Cu. Importantly, the broader SF distributions in the Cu- and Mg-containing alloys imply an increased likelihood of activating multiple slip systems, which would improve deformation compatibility and ductility—an advantageous feature for implants subjected to complex physiological loading.

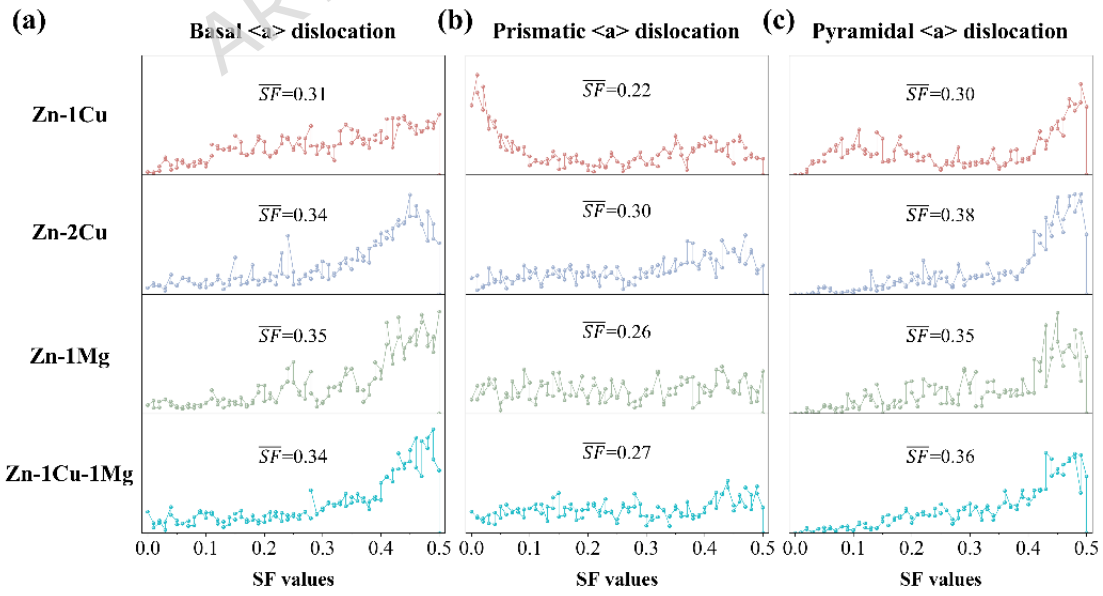

Figure 3: Schmid factors (SF) of Zn alloys. (a) Basal <a> dislocations. (b) Prismatic <a> dislocations. (c) Pyramidal <a>

dislocations.

3. 2 TEM characterization of nanoscale strengthening phases

TEM observations of the ECAP-processed Zn–1Cu–1Mg alloy revealed a high number density of finely dispersed particles (**Figure 4a**). These particles were distributed throughout the matrix and exhibited a characteristic size on the order of ~100 nm (**Figure 4b**). Selected-area electron diffraction (SAED) patterns (**Figure 4c**) identified the nanoparticles as $CuZn_4$. In addition, numerous dynamically recrystallized (DRX) grains and equiaxed Mg_2Zn_{11} particles were observed (**Figure 4d**), consistent with fragmentation of the as-cast eutectic constituents during severe plastic deformation. Notably, abundant nanoscale precipitates were also present within Mg_2Zn_{11} (**Figure 4e**). Diffraction rings in the corresponding SAED pattern (**Figure 4f**) were indexed to $MgZn_2$, in agreement with previous reports [26]. The nanoscale size and high dispersion density of these secondary phases provide a microstructural basis for the enhanced mechanical performance of Zn–1Cu–1Mg alloy.

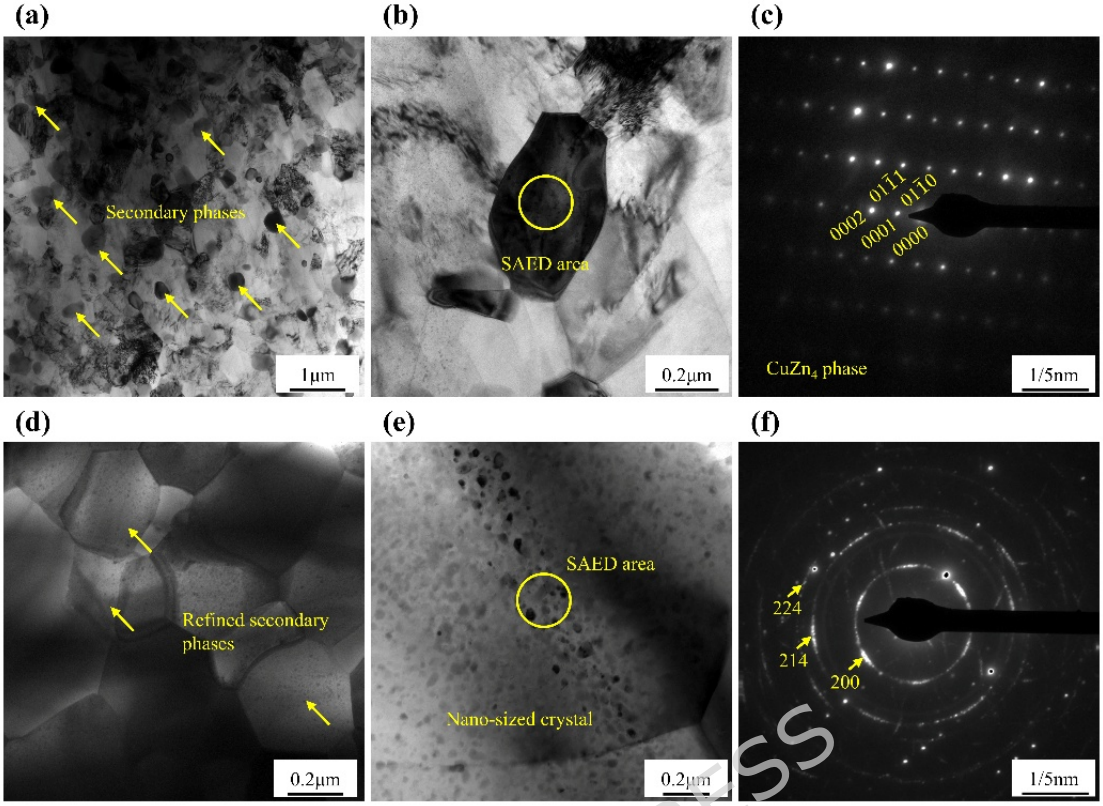

Figure 4: TEM images of the as-deformed Zn-1Cu-1Mg alloys. (a) Distributions of $CuZn_4$ particles. (b, c) Morphologies of particles and the corresponding SAED image. (d) Distributions of Mg_2Zn_{11} phases. (e, f) Nano-sized crystal within Mg_2Zn_{11} phases and the corresponding SAED image.

3.3. Mechanical and corrosion behaviors

To evaluate the mechanical performance of the ECAP-processed alloys, Vickers microhardness and uniaxial tensile tests were conducted. As shown in **Figure 5a**, Zn–1Cu exhibited a hardness of 71 ± 10 HV, which increased slightly to 77 ± 11 HV for Zn–2Cu. Zn–1Mg showed a substantially higher hardness (112 ± 14 HV) than the Zn–Cu alloys, indicating a stronger strengthening contribution from Mg. With the combined addition of Cu and Mg, hardness further increased to 129 ± 9 HV in Zn–1Cu–1Mg. This trend was consistent with the tensile results. The engineering stress–strain curves (**Figure 5b**) showed ultimate tensile strengths (UTS) of 232 MPa and

342 MPa for Zn–1Cu and Zn–1Mg, with corresponding elongations of 41.3% and 20.4%, respectively. These results indicate that Mg provides more pronounced strengthening than Cu, but at the expense of ductility. Importantly, introducing 1 wt.% Cu into Zn–1Mg increased the UTS to 424 MPa while improving elongation to 28.6%. Thus, Zn–1Cu–1Mg achieved a favorable strength–ductility balance, supporting its potential for load-bearing orthopedic fixation. Fractography (**Figure 5c**) indicated predominantly ductile failure across all compositions, characterized by fine and relatively uniform dimples. The improved ductility of Zn–1Cu–1Mg is plausibly associated with ultrafine grains and dispersed nanoscale precipitates, which promote more homogeneous load transfer and strain accommodation.

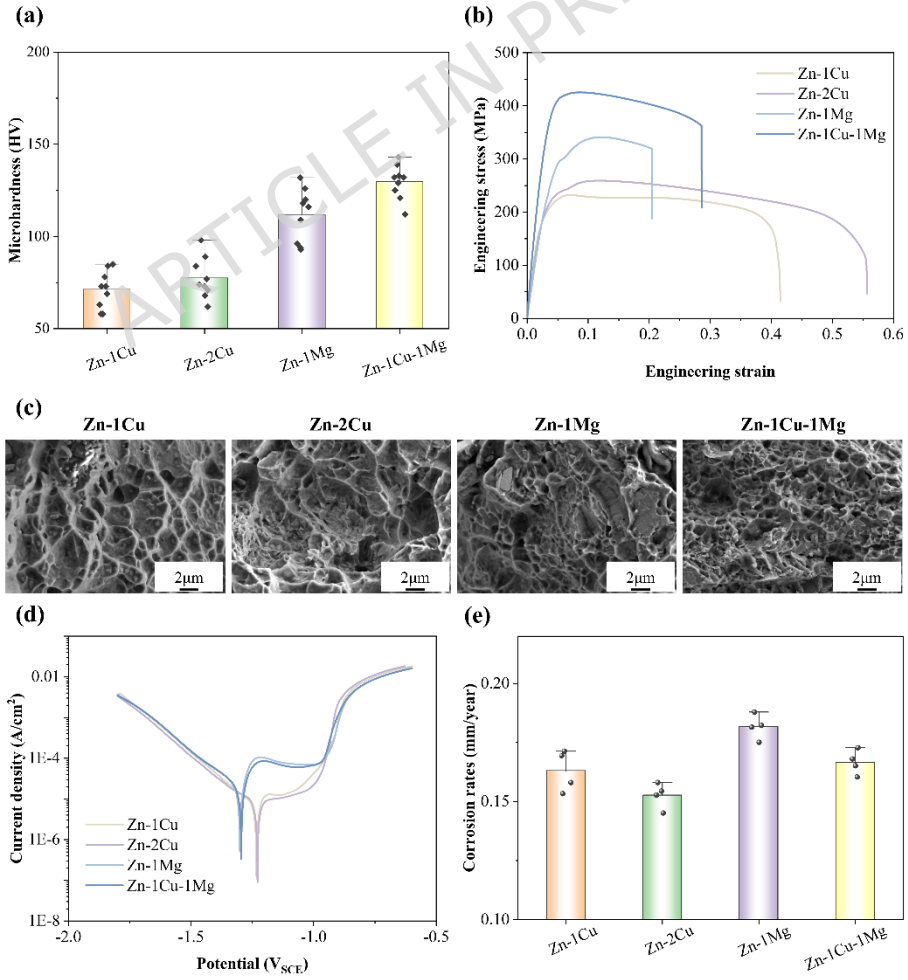

Figure 5: Mechanical and corrosion behaviors of as-deformed Zn alloys. (a) Microhardness. (b) Tensile curves. (c) Fracture morphologies. (d) PDP curves. (e) Corrosion rates.

Figure 5d presents the potentiodynamic polarization (PDP) curves of the as-deformed Zn alloys. The corrosion potential (E_{corr}) and corrosion current density (i_{corr}), determined using conventional Tafel extrapolation from the quasi-linear regions of the anodic and cathodic branches near E_{corr}, are summarized in **Table. 2**. The Zn-1Cu and Zn-2Cu alloys exhibited more positive E_{corr} at -1.23 ± 0.04 and -1.22 ± 0.08 V_{SCE}. The i_{corr} of Zn-1Cu and Zn-2Cu alloys were 6.19 ± 0.82 and 4.72 ± 0.96 μA/cm². After alloying with Mg element, E_{corr} shifted negatively, while i_{corr} progressively increased. For the Zn-1Mg alloy, its E_{corr} was -1.29 ± 0.06 V_{SCE} and i_{corr} was 15.61 ± 1.07 μA/cm². Addition of 1 wt.%Cu in Zn-1Mg alloys slightly shifted E_{corr} positively from -1.29 ± 0.06 V_{SCE} to -1.28 ± 0.03 V_{SCE} and reduced i_{corr} from 15.61 ± 1.07 μA/cm² to 14.65 ± 0.94 μA/cm². These results suggest that Mg promotes corrosion of Zn alloys. The addition of Cu to Zn-1Mg shows a slight reduction trend in i_{corr}; however, given the overlapping standard deviations, this difference cannot be conclusively regarded as statistically significant. Therefore, the effect of Cu should be interpreted as moderating corrosion behavior rather than definitively suppressing it.

Table. 2: Corrosion parameters obtained from PDP curves.

Samples	E_{corr} (V_{SCE})	i_{corr} (μA/cm^2)
Zn-1Cu	-(1.23 ± 0.04)	6.19 ± 0.82
Zn-2Cu	-(1.22 ± 0.08)	4.72 ± 0.96
Zn-1Mg	-(1.29 ± 0.06)	15.61 ± 1.07
Zn-1Cu-1Mg	-(1.28 ± 0.03)	14.65 ± 0.94

Immersion testing in Hank's solution further supported the electrochemical trends. As shown in **Figure 5e**, the corrosion rate of Zn–1Cu was 0.163 ± 0.008 mm·year^{-1} and decreased to 0.152 ± 0.006 mm·year^{-1} for Zn–2Cu. Zn–1Mg exhibited the highest corrosion rate (0.182 ± 0.005 mm·year^{-1}), which decreased to 0.167 ± 0.005 mm·year^{-1} after adding 1 wt.% Cu. Overall, Cu-containing alloys corroded more slowly than Mg-only alloys, consistent with improved corrosion resistance imparted by Cu.

After 30 days of immersion, SEM images revealed continuous corrosion product layers on all alloys (**Figure 6a**). Particle-like corrosion products were distributed across the surfaces with similar areal densities among the groups. EDS mapping of the corrosion layers (**Figure 6b**) showed enrichment of O, Cl, Ca, and P in micron-scale particles, whereas submicron particles were primarily enriched in C and O. After removing corrosion products, the underlying surfaces exhibited localized corrosion features (**Figure 6c**), including micrometer-scale pits. Notably, Cu-containing alloys displayed a reduced pit density compared with Mg-only alloys, indicating more controlled localized corrosion. Such moderated degradation is desirable for biodegradable implants, as it can help maintain mechanical integrity during early healing while allowing gradual resorption as infection resolves and bone regeneration proceeds.

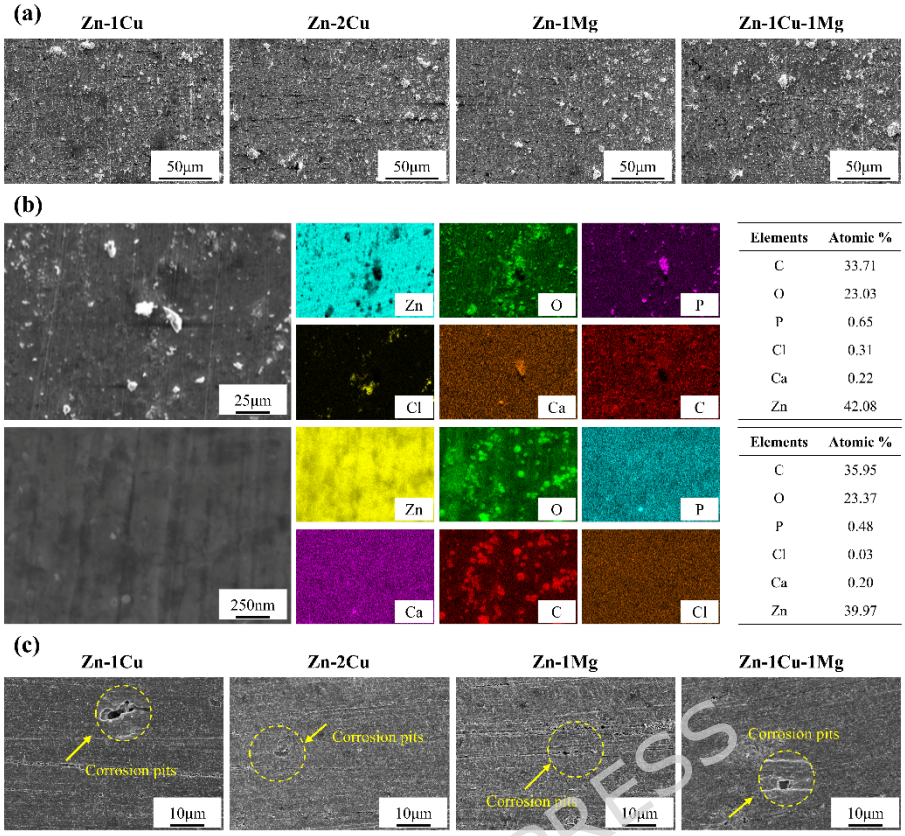

Figure 6: Surface morphologies of Zn alloys after immersion for 30 days. (a) SEM images before removing corrosion products. (b) Corrosion products and the corresponding EDS mappings. (c) SEM images after removing corrosion products.

3.4. Cytocompatibility with BMSCs

To evaluate biocompatibility, bone mesenchymal stem cells (BMSCs) were cultured in alloy extracts, with bioinert titanium (Ti) serving as a negative control. **Figure 7a** shows BMSC viability after 3 days of exposure to extracts at different concentrations. In undiluted (100%) extracts, all Zn-alloy groups initially exhibited lower metabolic activity than the Ti control. Notably, Zn–1Mg and Zn–1Cu–1Mg supported higher cell activity than the Zn–Cu alloys, which may be associated with reduced Zn^{2+} exposure and increased Mg^{2+} availability in the Mg-containing extracts. After 5 days of culture (**Figure 7b**), the Zn–Cu groups still showed comparatively lower

viability in both undiluted and diluted conditions. In contrast, the one-fold diluted (50%) extracts of Mg-containing alloys maintained high viability (>90%), and all alloys exhibited good cytocompatibility at the two-fold dilution (25%). Live/dead staining (**Figure 7c**) further demonstrated minimal cytotoxicity for Zn–1Mg and Zn–1Cu–1Mg extracts, indicating favorable biosafety for BMSC culture.

Ion concentrations in the undiluted extracts are summarized in **Figure 7d**. Zn–1Cu exhibited the highest Zn^{2+} concentration, while Zn–2Cu showed the highest Cu^{2+} level, which likely contributed to reduced cell viability. Alloying with Mg decreased Zn^{2+} concentration. Consistently, at 50% dilution, the reduction in Zn^{2+} was accompanied by improved BMSC viability relative to the undiluted condition. In some groups, viability exceeded 100%, further supporting the cytocompatibility of the extracts under appropriate dilution.

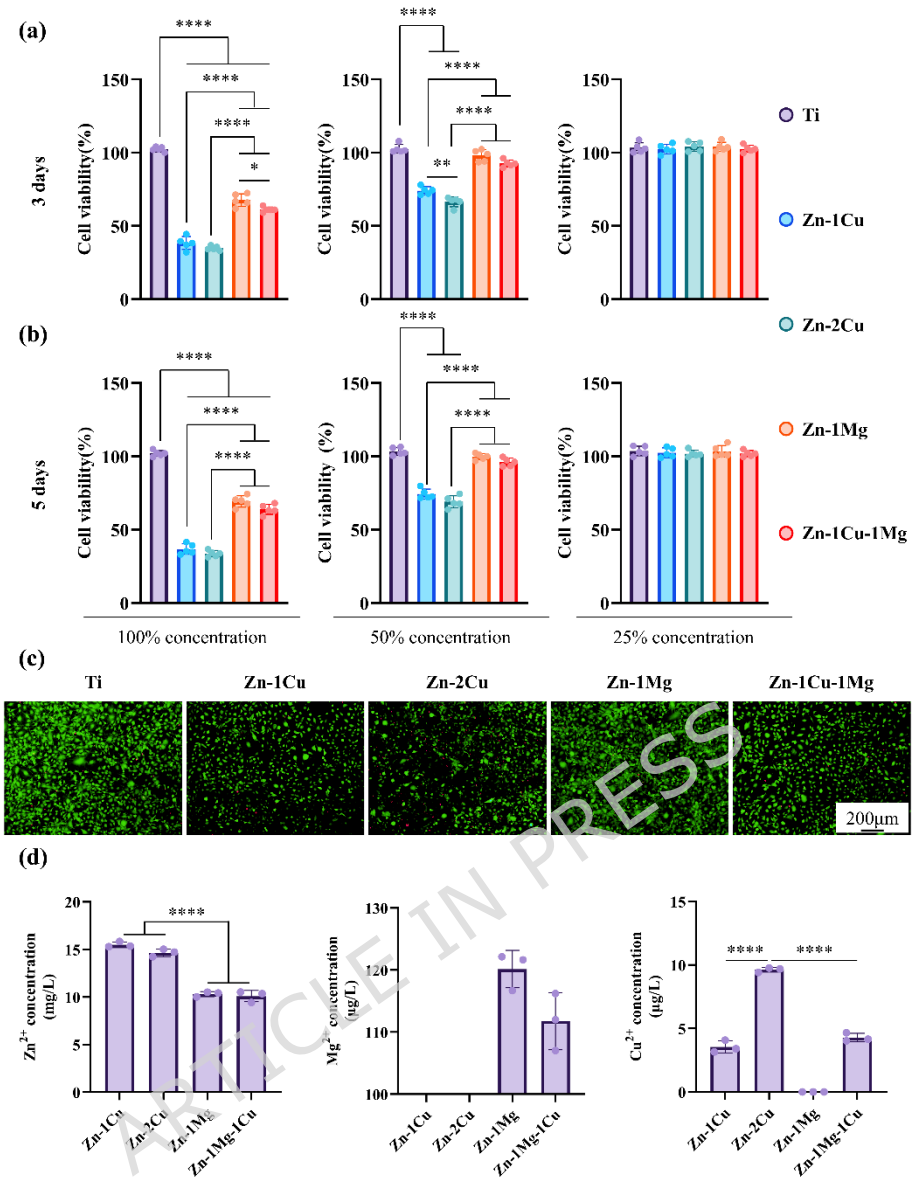

Figure 7: In vitro cytocompatibility of Zn alloys. (a) Cell viabilities to BMSCs after culturing for 3 days. From left to right, the concentrations of the extracts are 100%, 50%, and 25%. (b) Cell viabilities to BMSCs after culturing for 5 days. From left to right, the concentrations of the extracts are 100%, 50%, and 25%. (c) Live/dead images after culturing for 3 days. (Green = Live, Red = Dead). (d) Ionic concentrations in undiluted Zn alloy extracts. *p < 0.05, **p < 0.01, ****p < 0.0001.

3.5. Osteogenic activity

Early osteogenic potential was assessed using alkaline phosphatase (ALP) staining (days 7 and 14) and Alizarin Red S (ARS) staining (days 14 and 21) in BMSCs cultured in 50% alloy extracts. As shown in **Figure 8a** and **b**, ALP activity and ARS staining intensity were higher in the Zn-alloy groups than in the Ti control, indicating enhanced osteogenic differentiation and matrix mineralization. This response is attributed to the release of bioactive metal ions during degradation, which are known to regulate osteogenic signaling and mineral deposition. Among the tested compositions, Zn–1Mg and Zn–1Cu–1Mg induced more pronounced osteogenic responses than the Zn–Cu alloys, suggesting that elevated Mg^{2+} levels together with moderated Zn^{2+} concentrations create a more favorable osteoinductive microenvironment.

Gene expression analysis (**Figure 8e**) further supported these observations. Osteogenesis-related markers—including ALP, collagen I (COL1), Runx2, and osteopontin (OPN)—were upregulated in the Zn-alloy groups compared with the control, showing trends consistent with the staining results. Collectively, these findings indicate that the Zn-based alloys, particularly the Mg-containing compositions, promote osteogenic activity in BMSCs and are promising candidates for orthopedic applications.

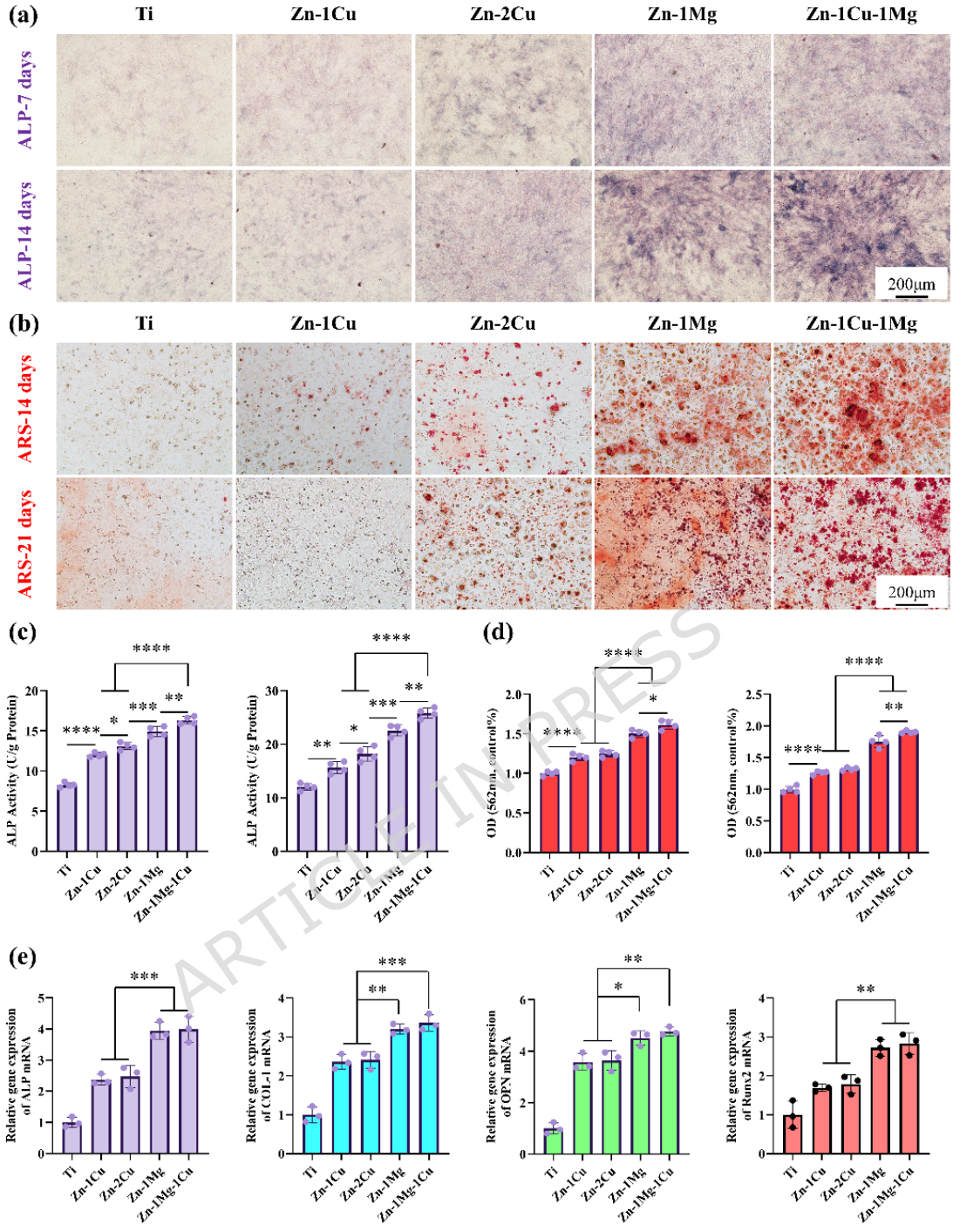

Figure 8: In vitro osteogenesis of Zn alloys. (a) ALP staining images. (b) ARS images. (c) ALP activities. (d) The mineralized nodule of BMSCs from ARS. (e) Relative expression of osteogenic differentiation marker genes. *p < 0.05, **p < 0.01, ***p < 0.001, ****p < 0.0001.

3.6. Antibacterial performance

The antibacterial activity of the alloys against *E. coli* and *S. aureus* is summarized in **Figure 9**. Numerous bacterial colonies were observed on Ti for both strains, confirming the lack of intrinsic antibacterial activity for bioinert Ti. In contrast, all Zn-based alloys reduced colony counts for both *E. coli* and *S. aureus*, indicating measurable antibacterial efficacy. At earlier time points, Zn–2Cu showed a lower *S. aureus* colony density than Zn–1Mg (**Figure 9c**), consistent with the antibacterial contribution of Cu. With prolonged incubation, the antibacterial effects among the Zn alloys became more comparable (**Figure 9d**), suggesting that sustained ion release and/or corrosion-associated microenvironmental changes contributed to antibacterial activity across compositions.

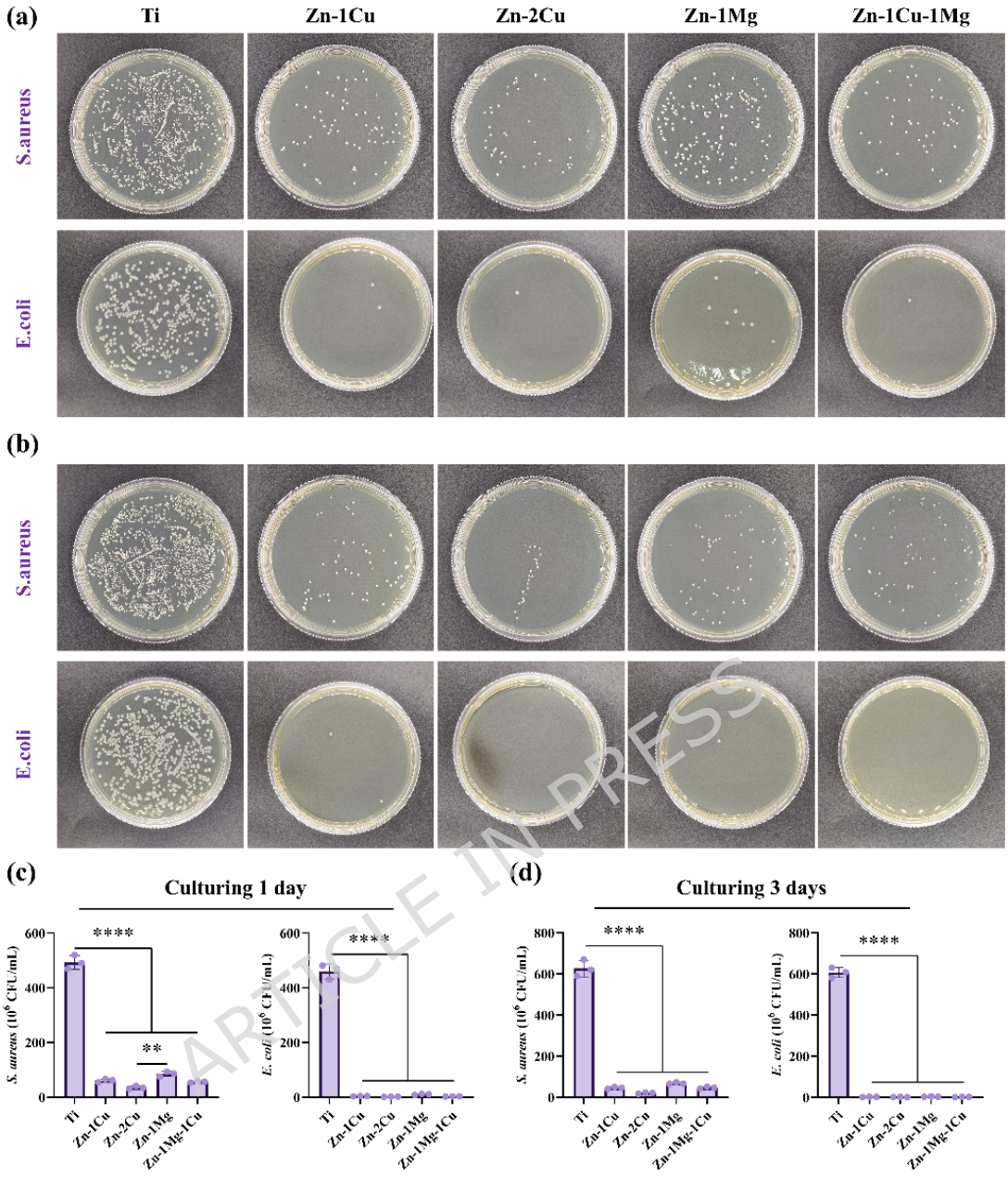

Figure 9: In vitro antibacterial capabilities of Zn alloys. Representative CFU images of bacteria growth after co-culturing for (a) 1 day, (b) 3 days. (c) CFU numbers of bacteria after co-culturing for (a) 1 day, (b) 3 days. ****$p < 0.0001$.

4. Discussions

This study shows that Zn-based alloys containing Cu and Mg can integrate antibacterial function, osteogenic stimulation, regulated

degradability, and improved mechanical performance, indicating strong promise as multifunctional biodegradable metals for osteomyelitis treatment. Systematic evaluations of microstructure, corrosion behavior, mechanical response, cytocompatibility, and antibacterial efficacy further clarify how alloy composition together with processing conditions jointly determines the performance of Zn–Cu–Mg systems. The discussion therefore focuses on (i) microstructure-driven strengthening and enhanced ductility, (ii) corrosion processes and the associated degradation rates, and (iii) how ion release mediates the balance between osteogenesis and antibacterial activity.

4.1. Improving mechanical properties by microstructural evolutions in Zn alloys

Micron-scale grain refinement often enables concurrent increases in strength and ductility in metals [33,34]. Here, the Zn grain size is reduced to 0.58 μm after Cu and Mg alloying. Prior work indicates that Zn–Cu alloys can achieve high elongation through multiple deformation modes [23,35], whereas ECAP-processed Zn–Mg alloys typically exhibit high strength but limited elongation due to brittle eutectic structures [36,37 38]. In line with this trend, the elongation of the Zn-1Cu-1Mg alloy is 140% higher than that of the Zn-1Mg alloy. As grain size decreases to the submicron scale, deformation behavior may shift toward enhanced grain-boundary-mediated accommodation mechanisms. [39,40]. Although classical grain-boundary sliding (GBS) is typically dominant at elevated temperatures or low strain rates, ultrafine grains at room temperature can facilitate cooperative grain-boundary activity and improved strain compatibility. In the present study, tensile testing was conducted at 1×10^{-3} s^{-1}, and strain-rate sensitivity was not

evaluated; therefore, we do not assert GBS as the dominant mechanism. Instead, the improved ductility is attributed to combined effects of grain refinement, texture weakening, and enhanced activation of multiple slip systems. Similar behavior has been reported in other Zn alloys: Jarzębska *et al.* showed that refining Zn-1Mg to 0.7 μm produced an elongation of 35% [41], and Bednarczyk *et al.* reported that refining Zn-0.5Cu to 1.32 μm enabled exceptionally high elongation under specific testing conditions [42]. It should be noted that elongation values are highly sensitive to strain rate and testing parameters. Since the present tensile tests were conducted at a fixed strain rate of 1×10^{-3} s^{-1}, direct numerical comparison with literature values obtained under different strain rates is not strictly valid. Therefore, the comparison here is intended to highlight general deformation trends associated with grain refinement rather than to equate absolute elongation values.

Secondary-phase particles influence recrystallization behavior in a size-dependent manner. Classical particle-stimulated nucleation (PSN) generally requires particles larger than ~1 μm to generate sufficient local lattice curvature [43]. In the present Zn–1Cu–1Mg alloy, ECAP processing fragmented the original eutectic structures into submicron to micron-scale particles, which may introduce local strain heterogeneity and facilitate recrystallization initiation in their vicinity. In contrast, the nanoscale (~100 nm) $CuZn_4$ and $MgZn_2$ precipitates observed by TEM primarily exert Zener pinning pressure, restricting grain boundary migration and stabilizing the refined grain structure rather than directly stimulating nucleation. A comparable effect has been observed in Zn-0.2Mg, where Mg2Zn11 particles facilitate recrystallization during tensile deformation [44]. As shown in Figure 2b, the Zn-1Cu-1Mg alloy

exhibits the highest fraction of submicron grains. With increasing particle dispersion, the microstructural evolution is governed by two competing mechanisms. Fragmented eutectic particles may contribute to localized strain gradients that assist recrystallization initiation, whereas nanoscale precipitates inhibit grain boundary migration through Zener pinning. The observed high fraction of dynamically recrystallized grains in Zn-1Cu-1Mg is therefore more reasonably attributed to severe plastic deformation-induced continuous dynamic recrystallization, with particle effects primarily stabilizing the ultrafine grain structure rather than directly driving nucleation. When recrystallization-induced softening outweighs work hardening from dislocation accumulation, alloy strength decreases while plasticity increases. Consistently, GND density maps show that GND density declines as grain size is reduced, reaching the lowest level in the Zn-1Cu-1Mg alloy. This decrease in dislocation density is attributed to continuous dynamic recrystallization. Overall, the coexistence of fragmented submicron particles and nanoscale precipitates results in a dual effect: localized strain accommodation that may assist recrystallization onset, and strong Zener pinning that suppresses excessive grain growth. This synergistic interaction explains the high fraction of ultrafine dynamically recrystallized grains without invoking classical PSN by nanoscale particles.

Texture modification is an effective strategy for improving room-temperature ductility and formability in hexagonal close-packed (HCP) metals [45]. In Zn (c/a ≈ 1.85), twinning behavior differs from that of Mg due to its higher axial ratio. Under tensile loading along the RD, grains with the c-axis parallel to RD experience c-axis tension, which does not favor compression-type twinning [46].

Therefore, the observed (0001) pole distribution near the RD is more reasonably interpreted in terms of basal slip activation and possible orientation rotation during severe plastic deformation, rather than dominant compressive twinning. Texture evolution subsequently alters the Schmid factor (SF) for basal slip. The SF distributions for basal <a> slip {0001}<11$\bar{2}$0> in the two alloys are shown in Figure 3. The Zn-1Cu alloy contains a higher proportion of grains with low SF values than the Zn-1Cu-1Mg alloy, suggesting that basal slip is more readily activated in the latter. Zn-1Mg and Zn-1Cu-1Mg alloys show similar SF values for basal, prismatic, and pyramidal <a> slip systems; therefore, the elongation difference between these two alloys may primarily arise from fragmentation of the eutectic structures. In addition, texture weakening also contributes to the improved elongation [47]. The Zn-1Cu-1Mg alloy presents a relatively weak (0001) basal texture, with a maximum intensity of 5.23 mrd, which is lower than that of the Zn-1Mg alloy. For hexagonal Zn, the primary extension twinning mode is {10$\bar{1}$2}<10$\bar{1}$1>, whereas {11$\bar{2}$0} corresponds to compression twinning. Given the applied tensile loading along RD in this study, grains with c-axis parallel to RD would experience tensile stress along the c-axis, suppressing compression twinning. Therefore, twinning activity at room temperature is likely limited compared with basal slip, and the texture evolution observed after ECAP and tensile deformation is mainly governed by slip-dominated plasticity and dynamic recrystallization. Beyond strength, adequate ductility is critical for formability and intraoperative handling of orthopedic implants, allowing shaping/bending without cracking and improving damage tolerance under complex loading during healing. The presence of dispersed nanoscale precipitates contributes to improved ductility

not by classical precipitation strengthening alone, but by promoting microstructural homogenization. After ECAP processing, coarse eutectic phases were fragmented into fine and uniformly distributed particles, which reduced stress concentration and suppressed crack initiation sites. Such refined precipitate dispersion facilitates more uniform plastic deformation and delays localized strain accumulation, thereby improving tensile elongation.

4.2. Appropriate corrosion rates for biodegradable implants

Earlier work has described the in vitro corrosion behavior of Zn alloys containing Mg and Cu [48,49]. A frequently used medium is simulated body fluid (SBF), whose ionic composition is similar to that of Hank's solution. During immersion, Zn dissolves through the anodic reaction [50]:

$$Zn \rightarrow Zn^{2+} + 2e^-$$

while hydroxide ions form via the cathodic oxygen reduction:

$$O_2 + H_2O + 2e^- \rightarrow 4OH^-$$

The resulting OH^- combines with Zn^{2+} to generate $Zn(OH)_2$, which can further transform into the more stable ZnO by reaction:

$$Zn(OH)_2 \rightarrow ZnO + H_2O$$

Chloride ions in the solution can destabilize the $Zn(OH)_2$ layer, facilitating dissolution and releasing Zn^{2+}, thereby accelerating Zn-alloy corrosion. At the early immersion stage, the main corrosion products are ZnO and $Zn(OH)_2$, consistent with the high O signal observed in EDS maps. As shown in Figure 6b, micrometer-scale corrosion particles exhibit high levels of Cl, Ca, and P, in addition to O. Under the local electric field, Cl^- migrates toward anodic areas and reacts with Zn^{2+}, OH^-, and $Zn(OH)_2$ to likely form

$Zn_5(OH)_8Cl_2{\cdot}H_2O$ through the reactions [51]:

$$5Zn^{2+} + 8OH^- + 2Cl^- + H_2O \rightarrow Zn_5(OH)_8Cl_2{\cdot}H_2O$$

And

$$5Zn(OH)_2 + 2Cl^- + H_2O \rightarrow Zn_5(OH)_8Cl_2{\cdot}H_2O + 2OH^-$$

The enrichment of Cl is therefore indicative of $Zn_5(OH)_8Cl_2{\cdot}H_2O$ formation. Beyond Cl^-, Hank's solution also contains PO_4^{3-} HPO_4^{2-}, HCO_3^-, and Ca^{2+}, which collectively resemble inorganic components of physiological fluids. Accordingly, the elevated P and Ca signals are attributed to phosphate deposition, including $Zn_3(PO_4)_2{\cdot}4H_2O$ by the reaction:

$$3Zn^{2+} + 2HPO_4^{2-} + 2OH^- + 2H_2O \rightarrow Zn_3(PO_4)_2{\cdot}4H_2O$$

and $Ca_3(PO_4)_2$ by the reaction:

$$3Ca^{2+} + 2PO_4^{3-} \rightarrow Ca_3(PO_4)_2$$

For submicron corrosion products, a strong C signal is detected, which is associated with $Zn_5(CO_3)_2(OH)_6$ produced by

$$5Zn^{2+} + 2HCO_3^- + OH^- \rightarrow Zn_5(CO_3)_2(OH)_6 + 2H_2O$$

Importantly, the presence of HPO_4^{2-} and HCO_3^- likely promotes the deposition of $Ca_3(PO_4)_2$ and $CaCO_3$, which can partially impede Cl^- attack and thereby slow the corrosion of Zn alloys.

Electrochemical tests together with immersion results show that Zn–Cu alloys possess better corrosion resistance than Zn–Mg-based alloys. The higher corrosion rate in the Mg-containing alloys is associated with microstructural changes, particularly the appearance of Mg-containing phases and grain refinement.

Literature reports that increasing Mg content in Zn–Mg alloys raises the corrosion rate [52,53], implying that Mg addition promotes Mg_2Zn_{11} formation and thus accelerates corrosion. In addition, the relationship between average grain size (d) and corrosion current density can be expressed as: $i_{corr} = A + Bd^{-0.5}$ [54]. Where A and B are constants, d is the average grain size. When i_{corr} is below 10 μA/cm², smaller grains may facilitate the development of a compact oxide film that improves corrosion resistance. In this study, i_{corr} is 6.19 ± 0.82 μA/cm² for the Zn-1Cu alloy and 4.72 ± 0.96 μA/cm² for the Zn-2Cu alloy, whereas Zn-1Mg and Zn-1Cu-1Mg show higher values of 15.61 ± 1.07 μA/cm² and 14.65 ± 0.94 μA/cm², respectively. These lower i_{corr} values for the Zn–Cu alloys support the formation of a dense oxide film during corrosion. Although grain refinement can promote more uniform surface film formation in certain alloy systems, the present results indicate that grain size is not the dominant factor controlling corrosion in Zn-Cu-Mg alloys. Notably, the Zn-1Cu-1Mg alloy exhibits the finest grain size yet shows higher corrosion rates than the Zn-Cu binary alloys. This suggests that the electrochemical activity and distribution of secondary phases play a more critical role in determining corrosion behavior than grain refinement alone. The incorporation of Mg introduces Mg_2Zn_{11} intermetallic phases, which create micro-galvanic coupling with the Zn matrix. These galvanic interactions accelerate anodic dissolution and override the potential passivation benefit associated with refined grains. Therefore, phase composition—particularly the presence of Mg-containing phases—constitutes the primary determinant of corrosion kinetics in this system.

Although Cu is electrochemically nobler than Zn and Cu-rich phases may act as local cathodes, the overall corrosion behavior of Zn–Cu

alloys results from competing micro-galvanic and passivation effects. In the present ECAP-processed alloys, $CuZn_4$ precipitates are refined and homogeneously dispersed, which reduces severe cathode-anode area mismatch and mitigates localized corrosion intensity. Meanwhile, surface analysis indicates the formation of corrosion products enriched in Zn, O, Ca, and P, suggesting the development of compact and chemically stable layers under physiological conditions. The combined effects of refined microstructure and stabilized corrosion products contribute to the relatively improved corrosion resistance of Zn–Cu alloys compared with Mg-containing alloys. Importantly, introducing Cu into the Zn-1Mg alloy moderates the corrosion behavior. While Mg addition increases the corrosion rate due to the formation of Mg-containing intermetallic phases that may act as micro-galvanic couples, the incorporation of Cu appears to promote the formation of a more compact and stable corrosion layer. As evidenced by EDS mapping (Figure 6b), the corrosion products in Zn-1Cu-1Mg are enriched in Zn, O, Ca, P, and Cl, suggesting the formation of protective phosphate- and carbonate-containing compounds. These deposits can partially hinder aggressive Cl^- attack and reduce pit propagation. Therefore, Cu addition does not simply enhance antibacterial performance, but also contributes to a more controlled degradation profile in Zn-Mg alloys, balancing mechanical integrity retention and biodegradability-an essential requirement for osteomyelitis implants.

4.3. Osteogenesis and antibacterial properties of Zn alloys

Antibacterial rates against *S. aureus* and *E. coli* were quantified and are summarized in **Table. 3**. All Zn alloys show antibacterial rates above 80% after 1 and 3 days of co-culture, indicating strong antimicrobial activity that is mainly associated with the broad-

spectrum effect of released Zn^{2+} ions [55,56]. Zn^{2+} can stimulate reactive oxygen species (ROS) generation, damage bacterial structures, interfere with intracellular metabolism and DNA replication, and thereby suppress bacterial growth and proliferation [57]. In addition, positively charged Zn^{2+} can adsorb onto bacterial membranes and compromise membrane integrity, leading to bacterial inactivation [58]. Overall, the antibacterial performance of Zn alloys generally increases with higher Zn^{2+} release [59]. A previous report found that the antibacterial rate against *S. aureus* reached ~80.6% when Zn^{2+} concentration was ~12.2 mg/L [60]. In the present work, undiluted extracts from the two Zn–Cu alloys contain 15.5 ± 0.3 mg/L and 14.7 ± 0.4 mg/L Zn^{2+}, both exceeding 12.2 mg/L, whereas Zn-1Mg releases 10.3 ± 0.3 mg/L Zn^{2+}. Consistent with these concentrations, the two Zn–Cu alloys exhibit stronger antibacterial effects than Zn-1Mg.

Table. 3: Antibacterial rates of Zn alloys

Samples	**Antibacterial rates**			
	Culturing for 1 day		Culturing for 3 days	
	S. aureus	*E. coli*	*S. aureus*	*E. coli*
Zn-1Cu	87.8 ± 1.6%	99.2 ± 0.2%	92.7 ± 0.7%	99.7 ± 0.2%
Zn-2Cu	92.9 ± 0.7%	99.6 ± 0.1%	96.8 ± 0.5%	99.8 ± 0.1%
Zn-1Mg	82.8 ± 2.3%	97.7 ± 0.6%	89.1 ± 0.1%	99.5 ± 0.2%
Zn-1Cu-1Mg	88.7 ± 0.5%	99.4 ± 0.1%	92.4 ± 1.2%	99.7 ± 0.1%

Beyond Zn^{2+}, Cu^{2+} also contributes to antibacterial action by binding to and inactivating proteins, altering membrane structure and permeability, promoting oxidative damage within microorganisms, and disrupting protein structures [61]. Accordingly, introducing Cu markedly enhances the antibacterial performance of the Zn-1Mg alloy. Moreover, the released Zn^{2+} from these Zn alloys shows strong inhibition of *E. coli*, with antibacterial rates reaching 99% as co-culture time is extended. The extent of improvement against *E. coli* is comparable to that against *S. aureus*, which may relate to differential ion tolerance among bacterial species.

As shown in **Figure 7**, despite the pronounced antibacterial activity of the Zn–Cu alloys, BMSC viability in 100% extracts is below 50%. This outcome reflects the dose dependence of BMSCs on Zn^{2+} and Cu^{2+} [62] : when ion concentrations rise beyond a tolerable range, BMSC proliferation is inhibited, leading to reduced viability [16]. Because ion levels in undiluted extracts exceed the cytocompatible threshold, diluted extracts are typically adopted to evaluate the cytotoxicity of biodegradable metals [63]. Notably, no cytotoxicity is detected when Zn-1Cu-1Mg extracts are diluted to 50%, suggesting that Mg^{2+} improves BMSC tolerance to Zn^{2+} and Cu^{2+}, effectively increasing the optimal concentration window. ALP and ARS assays further demonstrate superior osteogenic performance of Zn-1Cu-1Mg toward BMSCs, which is attributed to the co-release of Zn^{2+} and Mg^{2+} [64,65]. Consistently, PCR results show upregulated expression of osteogenic markers (OPN, COL-I, ALP, and RUNX-2), in agreement with prior studies [22,66]. Mechanistically, Zn^{2+} in diluted extracts can activate the PI3K–AKT pathway and thereby promote osteogenic differentiation of BMSCs [67]. Zn has also been reported to enhance osteogenesis by activating RUNX-2 via the cAMP–PKA–CREB

signaling axis [68]. In parallel, Mg^{2+} plays an important regulatory role in bone metabolism and regeneration; previous studies reported that Mg^{2+} promotes BMSC osteogenic differentiation by increasing ALP activity and elevating OPN and OCN levels [7]. Taken together, the combined effects of Zn^{2+} and Mg^{2+} underpin the enhanced osteogenic properties of the Zn-1Cu-1Mg alloy. The correlation between cytocompatibility and osteogenic differentiation suggests the existence of an optimal ionic microenvironment. Excessive Zn^{2+} and Cu^{2+} concentrations may suppress proliferation, thereby limiting the number of cells available for differentiation. In contrast, moderated Zn^{2+} release combined with Mg^{2+} supplementation appears to simultaneously sustain viability and promote osteogenic signaling pathways. This dual effect likely underlies the superior performance of Zn-1Cu-1Mg alloy. Therefore, the biological response is not solely concentration-dependent but reflects a balanced ion-mediated regulation of proliferation and differentiation processes. It should be noted that antibacterial assays were performed under direct-contact conditions, which allow localized ion accumulation at the implant–bacteria interface. In contrast, osteogenic differentiation was evaluated using diluted extracts to ensure cytocompatibility. These models simulate distinct biological environments—early infection control versus host tissue integration. Therefore, the dual-functionality described here reflects a design strategy to optimize the trade-off between antimicrobial efficacy and osteogenic support, rather than identical performance under identical dilution conditions.

5. Conclusions

This work indicates that the Zn-Cu, Zn-Mg and Zn-1Cu-1Mg alloys

integrates mechanical robustness, regulated biodegradation, favorable cytocompatibility, enhanced osteogenic potential, and inherent antibacterial performance. Microstructural analyses identified ultrafine grains together with nanoscale precipitates. The refined microstructures underpin the improved mechanical strength by grain boundary strengthening and secondary phase strengthening. Moreover, addition of Cu in Zn-1Mg alloys promotes the fragmentation of eutectic structures and weakens texture intensity, resulting in the improvement of elongation. Zn-1Mg alloy alloying with Cu reduces the corrosion rates, which is associated with the formation of compact corrosion layers enriched in Zn, O, C, Ca, P, and Cl. The Zn-1-Cu-1Mg alloy maintain BMSCs' viability and markedly promoted osteogenic differentiation, while effectively suppressing *S. aureus* and *E. coli*. Overall, these results suggest that Zn-based alloys may help address infection, a key constraint in current osteomyelitis management.

AUTHOR INFORMATION

Corresponding Author

Jin Xiao − *Department of Orthopedics, Guangdong Provincial People's Hospital (Guangdong Academy of Medical Sciences), Maoming People's Hospital, Southern Medical University, Guangzhou, 510080, P. R. China;*

Email: xiaojinhn@163.com. https://orcid.org/0000-0002-9919-7397

Guiying Liu − *Department of Cardiovasology, The Fifth Affiliated Hospital of Southern Medical University, No. 566 Congcheng*

Avenue, Conghua District, Guangzhou 510900, P. R. China;

Email: Liugy1987@163.com.

Yu Zhang − *Department of Orthopaedics Oncology, Guangdong Provincial People's Hospital (Guangdong Academy of Medical Sciences), Southern Medical University, Guangzhou, 519041 Guangdong, P.R. China;*

Email: luck_2001@126.com.

Authors

Jingzhe He − *Department of Orthopaedics Oncology, Guangdong Provincial People's Hospital (Guangdong Academy of Medical Sciences), Southern Medical University, Guangzhou, Guangdong 519041, P.R. China.*

Yindong Song − *Department of Orthopedics, Liwan Central Hospital of Guangzhou, Guangzhou, Guangdong 510170, P.R. China.*

Yi Xiao − *Division of Orthopaedic Surgery, Department of Orthopaedics, Nanfang Hospital, Southern Medical University, Baiyun Distrcit, Guangzhou, Guangdong 510515, China.*

Yifang Wang − *Department of Orthopaedic Surgery, The Third People's Hospital of Chengdu, Chengdu, Sichuan 610031, P.R. China.*

Yuan Yan − *Department of Orthopaedics Oncology, Guangdong Provincial People's Hospital (Guangdong Academy of Medical Sciences), Southern Medical University, Guangzhou, Guangdong 519041, P.R. China.*

Hui Yu − *Department of Orthopaedics Oncology, Guangdong Provincial People's Hospital (Guangdong Academy of Medical Sciences), Southern Medical University, Guangzhou, Guangdong*

519041, P.R. China.

Author Contributions

JZ.H., DY.S., and Y.X. contributed equally to this work. JZ.H., and DY.S. was responsible for conceptualization, methodology, investigation, and writing the original draft. Y.X. conducted methodology development, investigation (corrosion experiments, antibacterial testing), validation, data curation, and writing the original draft. YF.W. performed in vitro cytocompatibility assays, formal analysis, and visualization. Y.Y. carried out osteogenic induction experiments, sample preparation, and data collection. H.Y. provided resources, technical support, and validation. Y.Z. supervised the project, led conceptualization, performed writing – review & editing, and secured funding acquisition. J.X. and GY.L. provided supervision, designed the methodology, conducted writing – review & editing, and gave final approval of the manuscript. All authors have read and agreed to the published version of the manuscript.

Competing interests

The authors declare no competing financial interest.

Acknowledgements

None.

Funding

This study was supported by the Doctoral Research Startup Special Fund of People's Hospital of Dianbai District (MDH2025BSOS001).

Data availability statement

Data for this article, including generated or analyzed during this

study are available at figshare at https://doi.org/10.6084/m9.figshare.30816842.

Reference

1 Collet, Q., Velard, F., Laurent, F. & Josse, J. Intracellular Staphylococcus aureus in osteoblasts and osteocytes and its impact on bone homeostasis during osteomyelitis. *Bone* **198**, 117536, doi:https://doi.org/10.1016/j.bone.2025.117536 (2025).

2 Zhong, C., Wu, Y., Lin, H. & Liu, R. Advances in the antimicrobial treatment of osteomyelitis. *Composites Part B: Engineering* **249**, 110428, doi:https://doi.org/10.1016/j.compositesb.2022.110428 (2023).

3 Sohrabi, K. & Belczyk, R. Surgical Treatment of Diabetic Foot and Ankle Osteomyelitis. *Clinics in Podiatric Medicine and Surgery* **39**, 307-319, doi:https://doi.org/10.1016/j.cpm.2021.11.003 (2022).

4 Zheng, Y. F., Gu, X. N. & Witte, F. Biodegradable metals. *Materials Science and Engineering: R: Reports* **77**, 1-34, doi:10.1016/j.mser.2014.01.001 (2014).

5 Zhang, T. *et al.* Bridging biodegradable metals and biodegradable polymers: A comprehensive review of biodegradable metal–organic frameworks for biomedical application. *Progress in Materials Science* **155**, 101526, doi:https://doi.org/10.1016/j.pmatsci.2025.101526 (2026).

6 Zheng, Y. in *Biodegradable Metals and Their Medical Applications* (ed Yufeng Zheng) 1-32 (Elsevier, 2026).

7 Tsakiris, V., Tardei, C. & Clicinschi, F. M. Biodegradable Mg

alloys for orthopedic implants – A review. *Journal of Magnesium and Alloys* **9**, 1884-1905, doi:10.1016/j.jma.2021.06.024 (2021).

8 Lee, J.-W. *et al.* Long-term clinical study and multiscale analysis of in vivo biodegradation mechanism of Mg alloy. *Proceedings of the National Academy of Sciences* **113**, 716-721, doi:10.1073/pnas.1518238113 (2016).

9 Morsiya, C. A review on parameters affecting properties of biomaterial SS 316L. *Australian Journal of Mechanical Engineering* **20**, 803-813, doi:10.1080/14484846.2020.1752975 (2022).

10 Zheng, Y. in *Biodegradable Metals and Their Medical Applications* (ed Yufeng Zheng) 267-316 (Elsevier, 2026).

11 Bowen, P. K., Drelich, J. & Goldman, J. Zinc exhibits ideal physiological corrosion behavior for bioabsorbable stents. *Adv Mater* **25**, 2577-2582, doi:10.1002/adma.201300226 (2013).

12 Rahim, S. A. *et al.* Microstructural control of Zn alloy by melt spinning - A novel approach towards fabrication of advanced biodegradable biomedical materials. *Materials Science and Engineering: A* **934**, 148347, doi:https://doi.org/10.1016/j.msea.2025.148347 (2025).

13 Bandekian, S. *et al.* Additive manufacturing of zinc-based biomaterials: Fabrication, performance and property evaluation. *Journal of Materials Research and Technology* **36**, 5484-5508, doi:https://doi.org/10.1016/j.jmrt.2025.04.127 (2025).

14 Yang, H. *et al.* Biodegradable zinc-based metallic materials: Mechanisms, properties, and applications. *Progress in Materials Science* **157**, 101584, doi:https://doi.org/10.1016/j.pmatsci.2025.101584 (2026).

15 Imtiaz, H., Riaz, M., Anees, E., Bashir, F. & Hussain, T. Effects of copper micro-alloying on the degradation behavior, microstructure, and mechanical properties of Zn-1.5%Mg biodegradable alloys for implant applications. *Journal of Materials Research* **40**, 1076-1087, doi:10.1557/s43578-025-01557-z (2025).

16 Morath, L. *et al.* The biological effects of copper alloying in Zn-based biodegradable arterial implants. *Biomaterials Advances* **167**, 214112, doi:https://doi.org/10.1016/j.bioadv.2024.214112 (2025).

17 Wu, D., Huang, T. & Liu, Z. Mechanical response of high purity Zn wires with different diameters. *Materials Letters* **324**, doi:10.1016/j.matlet.2022.132635 (2022).

18 Pachla, W. *et al.* Structural and mechanical aspects of hypoeutectic Zn-Mg binary alloys for biodegradable vascular stent applications. *Bioact Mater* **6**, 26-44, doi:10.1016/j.bioactmat.2020.07.004 (2021).

19 Tang, Z. *et al.* Potential biodegradable Zn-Cu binary alloys developed for cardiovascular implant applications. *J Mech Behav Biomed Mater* **72**, 182-191, doi:10.1016/j.jmbbm.2017.05.013 (2017).

20 Qu, X. *et al.* Biodegradable Zn-Cu alloys show antibacterial activity against MRSA bone infection by inhibiting pathogen adhesion and biofilm formation. *Acta Biomater* **117**, 400-417, doi:10.1016/j.actbio.2020.09.041 (2020).

21 Cui, J. *et al.* 3D printed Zn-Cu alloy bone scaffolds via nanoparticle incorporation: Microstructural evolution and enhanced mechanical-antimicrobial-osteogenic properties. *Materials & Design* **261**, 115390, doi:https://doi.org/10.1016/j.matdes.2025.115390 (2026).

22 Zhao, D. *et al.* Material–Structure–Function Integrated Additive Manufacturing of Degradable Metallic Bone Implants for Load-Bearing Applications. *Advanced Functional Materials* **33**, 2213128, doi:https://doi.org/10.1002/adfm.202213128 (2023).

23 Yang, Y., Zhao, F., Cui, D. & Tan, Y. Achieving ultrahigh strength and ductility in biodegradable Zn-xCu alloys via hot-rolling and tailoring Cu concentration. *Materials Characterization*, **218** 114530, doi:https://doi.org/10.1016/j.matchar.2024.114530 (2024).

24 Zhang, M. *et al.* A biodegradable Zn-4Cu-2Se alloy with enhanced work-hardening, antibacterial, and anti-tumor properties for orthopedic applications. **202** 660-679, *Acta Biomaterialia*, doi:https://doi.org/10.1016/j.actbio.2025.06.028 (2025).

25 Valiev, R. Z. & Langdon, T. G. Principles of equal-channel angular pressing as a processing tool for grain refinement. *Progress in Materials Science* **51**, 881-981, doi:https://doi.org/10.1016/j.pmatsci.2006.02.003 (2006).

26 Liu, H. *et al.* Evolution of Mg–Zn second phases during ECAP at different processing temperatures and its impact on mechanical properties of Zn-1.6Mg (wt.%) alloys. *Journal of Alloys and Compounds* **811**, doi:10.1016/j.jallcom.2019.151987 (2019).

27 Wang, X., Ma, Y., Meng, B. & Wan, M. Effect of equal-channel angular pressing on microstructural evolution, mechanical property and biodegradability of an ultrafine-grained zinc alloy. *Materials Science and Engineering: A* **824**, doi:10.1016/j.msea.2021.141857 (2021).

28 Xu, Z. *et al.* Revealing the abnormal softening mechanisms of

Zn-xCu (x=2, 3) wrought alloys by gradually increasing ECAP numbers. *Materials Science and Engineering: A* **856**, 143962, doi:https://doi.org/10.1016/j.msea.2022.143962 (2022).

29 Ren, K. *et al.* Effect of ECAP temperature on formation of triple heterogeneous microstructure and mechanical properties of Zn–1Cu alloy. *Materials Science and Engineering: A* **826**, doi:10.1016/j.msea.2021.141990 (2021).

30 Yang, Z. *et al.* A high strength and ductility Zn–Cu–Mg alloy achieved by bandlike distribution of ultra-fine CuZn5 and Mg2Zn11 particles. *Materials Science and Engineering: A* **850**, doi:10.1016/j.msea.2022.143584 (2022).

31 Gaetke, L. M., Chow-Johnson, H. S. & Chow, C. K. Copper: toxicological relevance and mechanisms. *Archives of toxicology* **88**, 1929-1938, doi:10.1007/s00204-014-1355-y (2014).

32 Lee, H., Lee, I., Xu, X., Omori, T. & Kainuma, R. Revisiting the Phase Equilibria in the Cu-Zn Binary System. *Journal of Phase Equilibria and Diffusion* **45**, 304-317, doi:10.1007/s11669-023-01061-z (2024).

33 Figueiredo, R. B., Kawasaki, M. & Langdon, T. G. Seventy years of Hall-Petch, ninety years of superplasticity and a generalized approach to the effect of grain size on flow stress. *Progress in Materials Science* **137**, doi:10.1016/j.pmatsci.2023.101131 (2023).

34 Lin, H., Hua, P., Huang, K., Li, Q. & Sun, Q. Grain boundary and dislocation strengthening of nanocrystalline NiTi for stable elastocaloric cooling. *Scripta Materialia* **226**, 115227, doi:https://doi.org/10.1016/j.scriptamat.2022.115227 (2023).

35 Jarzebska, A. *et al.* Dynamic Recrystallization and Its Effect on Superior Plasticity of Cold-Rolled Bioabsorbable Zinc-Copper

Alloys. *Materials (Basel)* **14**, doi:10.3390/ma14133483 (2021).

36 Mostaed, E., Sikora-Jasinska, M., Drelich, J. W. & Vedani, M. Zinc-based alloys for degradable vascular stent applications. *Acta Biomater* **71**, 1-23, doi:10.1016/j.actbio.2018.03.005 (2018).

37 Huang, H. *et al.* A High-Strength and Biodegradable Zn–Mg Alloy with Refined Ternary Eutectic Structure Processed by ECAP. *Acta Metallurgica Sinica (English Letters)* **33**, 1191-1200, doi:10.1007/s40195-020-01027-x (2020).

38 Queyreau, S., Monnet, G. & Devincre, B. Orowan strengthening and forest hardening superposition examined by dislocation dynamics simulations. *Acta Materialia* **58**, 5586-5595, doi:10.1016/j.actamat.2010.06.028 (2010).

39 Zheng, R. *et al.* Transition of dominant deformation mode in bulk polycrystalline pure Mg by ultra-grain refinement down to sub-micrometer. *Acta Materialia* **198**, 35-46, doi:10.1016/j.actamat.2020.07.055 (2020).

40 Mostaed, E., Ardakani, M. S., Sikora-Jasinska, M. & Drelich, J. W. Precipitation induced room temperature superplasticity in Zn-Cu alloys. *Mater Lett* **244**, 203-206, doi:10.1016/j.matlet.2019.02.084 (2019).

41 Jarzębska, A. *et al.* A new approach to plastic deformation of biodegradable zinc alloy with magnesium and its effect on microstructure and mechanical properties. *Materials Letters* **211**, 58-61, doi:10.1016/j.matlet.2017.09.090 (2018).

42 Bednarczyk, W., Wątroba, M., Kawałko, J. & Bała, P. Can zinc alloys be strengthened by grain refinement? A critical evaluation of the processing of low-alloyed binary zinc alloys using ECAP. *Materials Science and Engineering: A* **748**, 357-366, doi:10.1016/j.msea.2019.01.117 (2019).

43 Huang, K., Marthinsen, K., Zhao, Q. & Logé, R. E. The double-edge effect of second-phase particles on the recrystallization behaviour and associated mechanical properties of metallic materials. *Progress in Materials Science* **92**, 284-359, doi:10.1016/j.pmatsci.2017.10.004 (2018).

44 Mollaei, N., Fatemi, S. M., Aboutalebi, M. R., Razavi, S. H. & Bednarczyk, W. Dynamic recrystallization and deformation behavior of an extruded Zn-0.2 Mg biodegradable alloy. *Journal of Materials Research and Technology* **19**, 4969-4985, doi:https://doi.org/10.1016/j.jmrt.2022.06.159 (2022).

45 Lou, D., Wang, L., Ren, Y., Li, H. & Qin, G. Textural evolution and improved ductility in Zn-0.2Mg-0.8Mn (wt%) alloys at different extrusion temperatures. *Journal of Alloys and Compounds* **860**, doi:10.1016/j.jallcom.2020.158530 (2021).

46 Liu, S., Kent, D., Doan, N., Dargusch, M. & Wang, G. Effects of deformation twinning on the mechanical properties of biodegradable Zn-Mg alloys. *Bioact Mater* **4**, 8-16, doi:10.1016/j.bioactmat.2018.11.001 (2019).

47 Li, X.-M. *et al.* Highly plastic Zn-0.3Ca alloy for guided bone regeneration membrane: Breaking the trade-off between antibacterial ability and biocompatibility. *Bioactive Materials* **42**, 550-572, doi:https://doi.org/10.1016/j.bioactmat.2024.08.049 (2024).

48 Su, L. *et al.* Corrosion behavior, antibacterial properties and in vitro and in vivo biocompatibility of biodegradable Zn-5Cu-xMg alloy for bone-implant applications. *Biomaterials Advances* **165**, 214000, doi:https://doi.org/10.1016/j.bioadv.2024.214000 (2024).

49 Palai, D., Siva Prasad, P., Satpathy, B., Das, S. & Das, K. Development of Zn-2Cu-xMn/Mg Alloys for Orthopedic

Applications: Mechanical Performance to In Vitro Degradation under Different Physiological Environments. *ACS Biomaterials Science & Engineering* **9**, 6058-6083, doi:10.1021/acsbiomaterials.3c00641 (2023).

50 Vojtech, D., Kubasek, J., Serak, J. & Novak, P. Mechanical and corrosion properties of newly developed biodegradable Zn-based alloys for bone fixation. *Acta Biomater* **7**, 3515-3522, doi:10.1016/j.actbio.2011.05.008 (2011).

51 Tong, X. *et al.* Impact of gadolinium on mechanical properties, corrosion resistance, and biocompatibility of Zn-1Mg-xGd alloys for biodegradable bone-implant applications. *Acta Biomater* **142**, 361-373, doi:10.1016/j.actbio.2022.02.015 (2022).

52 Mostaed, E. *et al.* Novel Zn-based alloys for biodegradable stent applications: Design, development and in vitro degradation. *J Mech Behav Biomed Mater* **60**, 581-602, doi:10.1016/j.jmbbm.2016.03.018 (2016).

53 Ye, L. *et al.* Effect of grain size and volume fraction of eutectic structure on mechanical properties and corrosion behavior of as-cast Zn–Mg binary alloys. *Journal of Materials Research and Technology* **16**, 1673-1685, doi:https://doi.org/10.1016/j.jmrt.2021.12.101 (2022).

54 Ralston, K. D., Birbilis, N. & Davies, C. H. J. Revealing the relationship between grain size and corrosion rate of metals. *Scripta Materialia* **63**, 1201-1204, doi:https://doi.org/10.1016/j.scriptamat.2010.08.035 (2010).

55 Su, Y. *et al.* Enhanced cytocompatibility and antibacterial property of zinc phosphate coating on biodegradable zinc materials. *Acta Biomater* **98**, 174-185, doi:10.1016/j.actbio.2019.03.055 (2019).

56 Wang, Y.-W. *et al.* Superior Antibacterial Activity of Zinc Oxide/Graphene Oxide Composites Originating from High Zinc Concentration Localized around Bacteria. *ACS Applied Materials & Interfaces* **6**, 2791-2798, doi:10.1021/am4053317 (2014).

57 Ning, C. *et al.* Concentration ranges of antibacterial cations for showing the highest antibacterial efficacy but the least cytotoxicity against mammalian cells: implications for a new antibacterial mechanism. *Chemical research in toxicology* **28**, 1815-1822, doi:10.1021/acs.chemrestox.5b00258 (2015).

58 Pasquet, J. *et al.* The contribution of zinc ions to the antimicrobial activity of zinc oxide. *Colloids and Surfaces A: Physicochemical and Engineering Aspects* **457**, 263-274, doi:https://doi.org/10.1016/j.colsurfa.2014.05.057 (2014).

59 Wang, B. *et al.* Electrodeposited dopamine/strontium-doped hydroxyapatite composite coating on pure zinc for anti-corrosion, antimicrobial and osteogenesis. *Materials Science and Engineering: C* **129**, 112387, doi:https://doi.org/10.1016/j.msec.2021.112387 (2021).

60 Tao, B. *et al.* Zn-incorporation with graphene oxide on Ti substrates surface to improve osteogenic activity and inhibit bacterial adhesion. *Journal of Biomedical Materials Research Part A* **107**, 2310-2326, doi:https://doi.org/10.1002/jbm.a.36740 (2019).

61 Khan, T., Date, A., Chawda, H. & Patel, K. Polysaccharides as potential anticancer agents—A review of their progress. *Carbohydrate Polymers* **210**, 412-428, doi:https://doi.org/10.1016/j.carbpol.2019.01.064 (2019).

62 Ma, J., Zhao, N. & Zhu, D. Bioabsorbable zinc ion induced biphasic cellular responses in vascular smooth muscle cells.

Scientific Reports **6**, 26661, doi:10.1038/srep26661 (2016).

63 Bao, G. *et al.* Feasibility evaluation of a Zn-Cu alloy for intrauterine devices: In vitro and in vivo studies. *Acta Biomater* **142**, 374-387, doi:10.1016/j.actbio.2022.01.053 (2022).

64 Aljabr, R. Y. & Bose, P. S. C. Microstructural Evolution and Mechanical Performance of Magnesium-Niobium Composites with Potential for Biomedical Applications. *JOM* **77**, 2779-2796, doi:10.1007/s11837-025-07198-1 (2025).

65 Aljabr, R. Y., Verma, S. K. & Bose, P. Corrosion behavior and mechanical performance of Mg-Hydroxyapatite nanocomposites for biodegradable implants: The role of nanoparticle concentration and dispersion. *Proceedings of the Institution of Mechanical Engineers, Part E: Journal of Process Mechanical Engineering*, 09544089251396672, doi:10.1177/09544089251396672 (2025).

66 Xu, J. *et al.* An adaptive biodegradable zinc alloy with bidirectional regulation of bone homeostasis for treating fractures and aged bone defects. *Bioactive Materials* **38**, 207-224, doi:https://doi.org/10.1016/j.bioactmat.2024.04.027 (2024).

67 Yang, H. *et al.* Zn-0.4Li alloy shows great potential for the fixation and healing of bone fractures at load-bearing sites. *Chemical Engineering Journal* **417**, doi:10.1016/j.cej.2021.129317 (2021).

68 Park, K. H. *et al.* Zinc Promotes Osteoblast Differentiation in Human Mesenchymal Stem Cells Via Activation of the cAMP-PKA-CREB Signaling Pathway. *Stem Cells and Development* **27**, 1125-1135, doi:10.1089/scd.2018.0023 (2018).